Cement & Concrete Composites 35 (2013) 59–70

Contents lists available at SciVerse ScienceDirect

Cement & Concrete Composites

journal homepage: www.elsevier.com/locate/cemconcomp

Computational thermal homogenization of concrete

T. Wu [a,*], İ. Temizer [b], P. Wriggers [a]

[a] Institute of Continuum Mechanics, Leibniz Universität Hannover, Appelstraße 11, Hannover 30167, Germany
[b] Department of Mechanical Engineering, Bilkent University, Ankara 06800, Turkey

ARTICLE INFO

Article history:
Received 7 March 2012
Received in revised form 20 August 2012
Accepted 22 August 2012
Available online 16 September 2012

Keywords:
Multiscale
Thermal homogenization
Concrete

ABSTRACT

Computational thermal homogenization is applied to the microscale and mesoscale of concrete sequentially. Microscale homogenization is based on a 3D micro-CT scan of hardened cement paste (HCP). Mesoscale homogenization is carried out through the analysis of aggregates which are randomly distributed in a homogenized matrix. The thermal conductivity of this matrix is delivered by the homogenization of HCP, thereby establishing the link between micro-mesoscale of concrete. This link is critical to capture the dependence of the overall conductivity of concrete on the internal relative humidity. Therefore, special emphasis is given to the effect of relative humidity changes in micropores on the thermal conductivity of HCP and concrete. Each step of homogenization is compared with available experimental data.

1. Introduction

Concrete is an extremely complex heterogeneous material, requiring the design and analysis of macroscale structures to address its multiscale nature. The mesoscale of concrete consists of a binding matrix, aggregates and pores with broad size distributions as well as interfacial zones between the aggregates and the matrix. In this work, the mesoscale of concrete will be idealized by aggregates with a prescribed size distribution and the hardened cement paste (HCP) as the binding matrix, as illustrated in Fig. 1. On the other hand, the microscale will be represented by the microstructure of HCP, which is comprised of hydration products, unhydrated residual clinker and micropores.

In nature, the progression of various chemical reactions in concrete, such as alkali silica reaction [1] and alkali carbonate reaction [2], is under control of the temperature, and those reactions may occur at different length scales of concrete. Accordingly, a comprehensive understanding of the thermal conductivity at the relevant length scales, which controls the temperature distribution throughout the macroscopic structure under daily environmental conditions, is worth investigating. Traditionally, the macroscopic thermal conductivity of concrete is obtained through a conventional laboratory experiment, naturally taking into account all the inhomogeneities embedded at various scales throughout the specimen. However, such experiments are often expensive and cannot be carried out with complete flexibility in the loading conditions. Homogenization offers an alternative experimental approach in a virtual setting for macroscopic thermal characterization without the aforementioned shortcomings.

In the early years, analytical estimates for the effective properties of heterogeneous materials were first developed by Voigt [3], Reuss [4] and Hill [5]. Other classical models have been established to estimate effective properties, including the self-consistent method or the Mori–Tanaka method [6–8]. Unfortunately, most analytical estimates are motivated by simple microstructural geometries. Therefore, it is advantageous to develop and apply computational homogenization approaches that can handle arbitrarily complex microstructural geometries.

The computational homogenization approach is widely utilized in the multiscale analysis of heterogeneous materials by obtaining the effective physical properties of an equivalent homogeneous material to substitute for the heterogeneous one. This approach significantly depends on identifying a statistically representative volume element (RVE). Computational homogenization analysis in the mechanical regime is well-established, see [9–12]. This approach has also been extended to the thermal field with a variety of applications. Asakuma et al. [13] calculated the effective thermal conductivity of the metal hydride bed. It was also applied to open-cell metallic foams by Laschet et al. [14]. Zhang et al. [15] obtained the effective thermal conductivity of granular assemblies based on the discrete element method. In addition, a second-order thermal homogenization framework with higher-order fluxes was proposed by Temizer and Wriggers [16] to capture absolute size effects when the RVE size is not sufficiently small compared to a representative macrostructural length scale. The goal of the present work is to apply the computational thermal homogenization approach to identify the macroscopic thermal conductivity of

* Corresponding author. Tel.: +49 511 176 4118; fax: +49 511 762 5496.
E-mail address: wu@ikm.uni-hannover.de (T. Wu).

0958-9465/$ - see front matter
http://dx.doi.org/10.1016/j.cemconcomp.2012.08.026

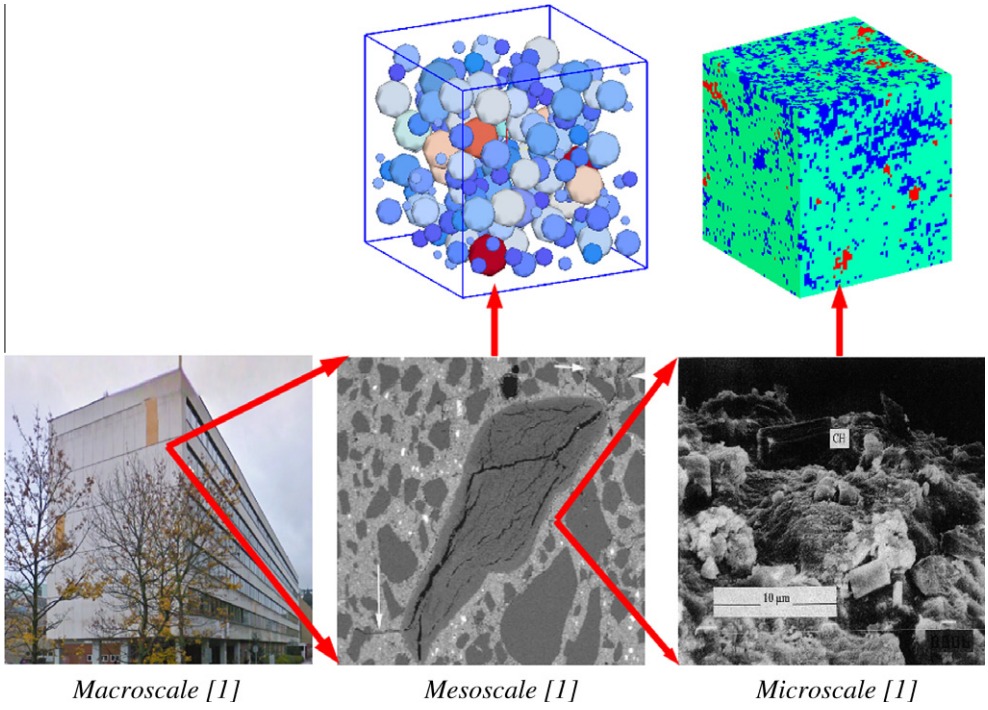

Fig. 1. Multiscale representation of concrete: macroscale–mesoscale–microscale.

concrete and investigate the effect of the variation of relative humidity in micropores on the macroscopic thermal conductivity.

This paper contains six sections. After Section 1, the basic principle of computational thermal homogenization is explained in Section 2. Section 3 describes computational thermal homogenization of HCP. The effect of relative humidity changes in micropores on the effective thermal conductivity of HCP is addressed in Section 4. Section 5 illustrates the homogenization framework in the mesoscale of concrete, where the effective thermal conductivity of HCP upscales microscale investigations to the mesoscale, which also takes into account the effect of the water content. Section 6 concludes with a summary and an outlook.

2. Computational thermal homogenization

2.1. Governing equation in the microscale

Fourier's law is assumed to be valid for each component in the microscale of concrete:

$$\mathbf{q} = -\mathbf{K} \cdot \nabla\theta \tag{1}$$

Here, $\mathbf{q}$ is the thermal flux, $\mathbf{K}$ is the symmetric thermal conductivity tensor and θ is the temperature. The isotropic thermal conductivity matrix is represented in the matrix form:

$$\mathbf{K} = \begin{bmatrix} K_{iso} & 0 & 0 \\ 0 & K_{iso} & 0 \\ 0 & 0 & K_{iso} \end{bmatrix}$$

Boundary conditions are prescribed through

$$\partial R^{\theta} \cup \partial R^{h} = \partial R, \quad \partial R^{\theta} \cap \partial R^{h} = \emptyset \tag{2}$$

$$\theta = \bar{\theta} \quad \text{on} \quad \partial R^{\theta}, \quad h = -\mathbf{q} \cdot \mathbf{n} = \bar{h} \quad \text{on} \quad \partial R^{h} \tag{3}$$

where h is the normal thermal flux, to bed used for the stationary problem of $-div(\mathbf{q}) = 0$.

2.2. Basis of computational thermal homogenization

Computational homogenization is a multiscale approach where the macroscale material response is obtained from an RVE. A sample from the heterogeneous material qualifies as an RVE when it is small enough compared to the macrostructural dimensions, yet it contains sufficient statistical information about the microstructure so as to accurately represent the response that the heterogeneous material exhibits on the macroscale [9–12]. A direct resolution of the fine scale representation of the whole domain is an alternative approach, albeit one that is prohibitively expensive due to computational demands that can easily exceed available resources. In computational thermal homogenization, an effective thermal conductivity matrix $\mathbf{K}^{*}$ is introduced to map the volume average of temperature gradient $\langle\nabla\theta\rangle$ to the volume average of thermal flux $\langle\mathbf{q}\rangle$

$$\langle\mathbf{q}\rangle = -\mathbf{K}^{*}\langle\nabla\theta\rangle \tag{4}$$

where the volume average of a quantity $\langle\bullet\rangle$ is defined

$$\langle\bullet\rangle = \frac{1}{|\Omega|}\int_{\Omega} \bullet \Omega \tag{5}$$

with Ω as the analysis volume.

2.3. Boundary conditions of thermal homogenization

Boundary conditions prescribed on the RVE have to satisfy the Hill criterion for a more reliable homogenization:

$$-\langle\mathbf{q} \cdot \nabla\theta\rangle = -\langle\mathbf{q}\rangle \cdot \langle\nabla\theta\rangle \tag{6}$$

This requirement, also called the Hill-Mandel condition [17], demonstrates the equivalence of averaged thermal dissipation and the thermal dissipation of the averages. In other words, this criterion indicates that the dissipation is preserved while making the transition from the microscale to the macroscale. A typical boundary condition satisfying the Hill criterion is the linear temperature boundary condition with a constant prescribed

temperature gradient $\nabla\theta_0$ on the RVE, so that the volume average of gradient temperature $\langle\nabla\theta\rangle$ of RVE is equal to the constant prescribed temperature gradient $\nabla\theta_0$. On the other hand, thermal flux boundary condition with a constant prescribed thermal flux $\mathbf{q}_0$ on the RVE can also be proven to satisfy the Hill criterion. In this case, one can show that the volume average of thermal flux $\langle\mathbf{q}\rangle$ of the RVE is equivalent to the prescribed thermal flux $\mathbf{q}_0$ [17]. Regarding specific derivations, the reader is referred to [17]. Note that the boundary conditions for homogenization have to satisfy the Hill criterion in order to support the homogenization procedure on physical grounds.

2.4. Numerical thermal homogenization procedure

Effective thermal conductivity K^*_{iso} for the isotropic case is determined by minimizing a least-square function [18]

$$\Pi := [\langle\mathbf{q}\rangle - \mathbf{q}^*(\langle\nabla\theta\rangle)]^2 \;\rightarrow\; min \tag{7}$$

in which the effective constitutive equation is defined through:

$$\mathbf{q}^*(\langle\nabla\theta\rangle) = -\begin{bmatrix} K^*_{iso} & & \\ & K^*_{iso} & \\ & & K^*_{iso} \end{bmatrix}\langle\nabla\theta\rangle \tag{8}$$

Differentiation of Eq. (7) with respect to K^*_{iso} yields the isotropic effective thermal conductivity:

$$K^*_{iso} = -\frac{\langle\mathbf{q}\rangle_1\langle\nabla\theta\rangle_1 + \langle\mathbf{q}\rangle_2\langle\nabla\theta\rangle_2 + \langle\mathbf{q}\rangle_3\langle\nabla\theta\rangle_3}{\langle\nabla\theta\rangle_1^2 + \langle\nabla\theta\rangle_2^2 + \langle\nabla\theta\rangle_3^2} \tag{9}$$

2.5. Effective thermal constitutive equation

Once the process of computational homogenization is carried out, the effective thermal constitutive equation is obtained

$$\mathbf{q}^* = -\mathbf{K}^*\cdot\nabla\theta^* \tag{10}$$

Boundary conditions are prescribed through

$$\theta^* = \bar{\theta} \quad on \quad \partial R^\theta \tag{11}$$

$$h^* = -\mathbf{q}^*\cdot\mathbf{n} = \bar{h} \quad on \quad \partial R^h \tag{12}$$

where $(*)$ denotes the effective quantity, to solve $-div(\mathbf{q}^*) = 0$ that characterizes a macroscopic problem.

3. Computational homogenization in the microscale

3.1. Hardened cement paste

HCP is a porous material comprised of hydration products, unhydrated residual clinker and micropores [19–21]. Specifically speaking, the main component of hydration product is calcium–silicate–hydrate (CSH), which is the main binding phase of all portland cement-based materials. Due to the variability of its chemical composition, the structure of hydration product is not clearly known. On the other hand, the main components of unhydrated residual clinker are C_3S, C_2S, C_3A and C_4AF [21,22], where in the standard cement chemistry the notation C stands for CaO, S for SiO_2 and A for Al_2O_3. According to the chemical observations [23], the thermal property of C_3S is very close to the cement powder, therefore, the thermal conductivity of the cement power will be substituted for C_3S in the computations. Another assumption in [23] proposes that micropores are full of water, hence, the thermal conductivity of water can ideally be used for micropores. In addition, 1 unit of C_3S reacts with 1.3 units of water to form 2.3 units of hydration products [22]:

Table 1
Thermal conductivity of components in HCP.

Material	Thermal conductivity (W/m K)
Hydration product	1.015
Unhydrated clinker	1.55 [23]
Micropore	0.604 [23]

$$\underset{1}{C_3S} + \underset{1.3}{5.3H} \rightarrow \underset{(2.3)}{C_{1.7}SH_4} + 1.3CH \tag{13}$$

Due to lack of experimental data, one assumes the thermal conductivity of hydration product through the volumetric weighted average of the water and clinker values

$$K_{HP} = \left(\frac{1}{2.3}\right)\times 1.55 + \left(\frac{1.3}{2.3}\right)\times 0.604 = 1.015 \text{ (W/m K)} \tag{14}$$

where K_{HP} is the thermal conductivity of hydration product. The thermal conductivities of the micropore and unhydrated clinker are presented in Table 1.

Considering an ordinary portland cement paste, the volume fractions of components in the HCP are evaluated through Power's hydration model [24]

$$V_M = \frac{w/c - 0.36h}{w/c + 0.32} \tag{15}$$

$$V_U = \frac{0.32(1-h)}{w/c + 0.32} \tag{16}$$

where w/c stands for the water-cement ratio, h for the hydration degree, V_M for the volume fraction of micropores and V_U for the volume fraction of unhydrated clinker residual. With $h = 0.945$ and $w/c = 0.45$ in this work, the volume fraction of hydration products is 84%, the one of unhydrated is 2% and the one of micropores is 14%.

3.2. Finite element representation of HCP

Computer Tomography (CT) is a non-destructive evaluation technique for producing 2D and 3D images of a specimen through X-ray, which originates from medical applications. Most medical tomographies have a resolution in the range of 1–3 mm, but micro-tomography can provide a resolution of approximately 1 μm for a three-dimensional specimen. In this way, one can study the microstructure of the material, which enables the numerical simulation in the microscale of the material. In this contribution, a micro-CT scan with an edge length of 1750 μm and a resolution of 1 μm was employed for HCP with $h = 0.945$ and $w/c = 0.45$ [20,25]. With the values of water-cement ratio and hydration degree, the volume fractions of components in the specimen of HCP are obtained through Eqs. (15) and (16). Micro-CT scan of HCP is comprised of 1750^3 data points, where each point corresponds to a voxel of 1 μm^3. With the underlying voxel data structure, the natural element to use within the finite element method to discretize the microstructure is an 8-node brick where each element is assigned to a single material phase. This choice allows a straightforward transition from the micro-CT scan data to the numerical analysis stage. The representation of HCP is shown in Fig. 2, in which the green[1] sections are hydration products, the blue sections are micropores and the red sections are unhydrated residual clinker, which has already been applied in the mechanical field and diffusion field, see [18,20,25]. Alternatively, microstructure development of

[1] For interpretation of color in Figs. 2 and 10, the reader is referred to the web version of this article.

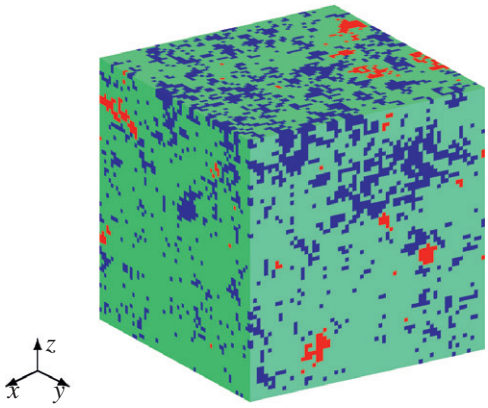

Fig. 2. Micro-CT-scan image of HCP with voxel dimension of $64 \times 64 \times 64\ \mu m^3$.

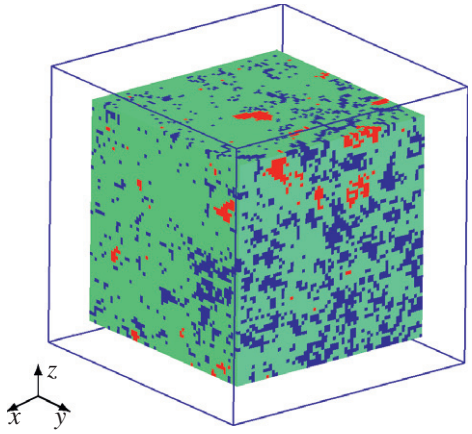

Fig. 3. Sample of HCP embedded in a window (window shown).

HCP could be simulated using, for example, the cellular automata-based program CemHyd3D from NIST [26].

3.3. Simulation results in the microscale

When boundary conditions are imposed directly on the boundary of RVE, problems of nonequilibrium and unnatural thermal flux may occur due to different materials on the surface of the sample. The window method [20] can overcome this problem. The idea is to embed the RVE in a homogeneous medium with a certain thickness (see Fig. 3) and an initial choice for its thermal conductivity is made. Linear temperature or uniform flux boundary conditions are directly prescribed on the window. One then obtains a new effective conductivity of the RVE, which is assigned to the window in a new iteration step. These iterations are performed until the change of the effective conductivity from one step to the next one is sufficiently small, thereby satisfying the condition of self-consistency. The thermal flux in the hydration products of HCP obtained using linear temperature boundary conditions without and with window is shown in Figs.4 and 5 respectively, where the thermal flux distribution is more even and realistic after using the window method.

The size of the analysis sample critically affects the accuracy of the homogenization results. The macroscopic property of a small sample varies considerably depending on the chosen portion of the micro-CT scan. In other words, a single small sample is not accurate enough to capture the macroscopic response. Statistical tests using randomly chosen portions from the micro-CT scan can overcome this drawback. Fig. 6 illustrates the mean value of

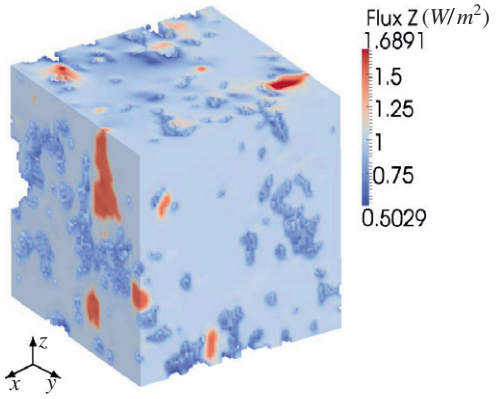

Fig. 4. Thermal flux in hydration products of HCP without window method.

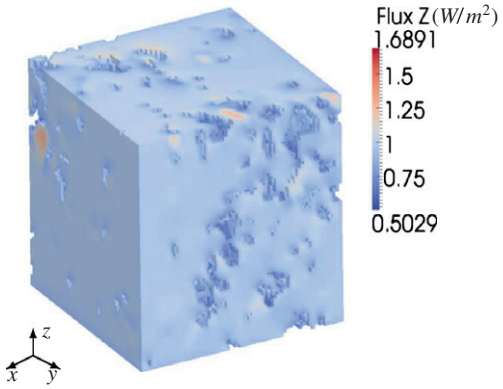

Fig. 5. Thermal flux in hydration products of HCP with window method (window not shown).

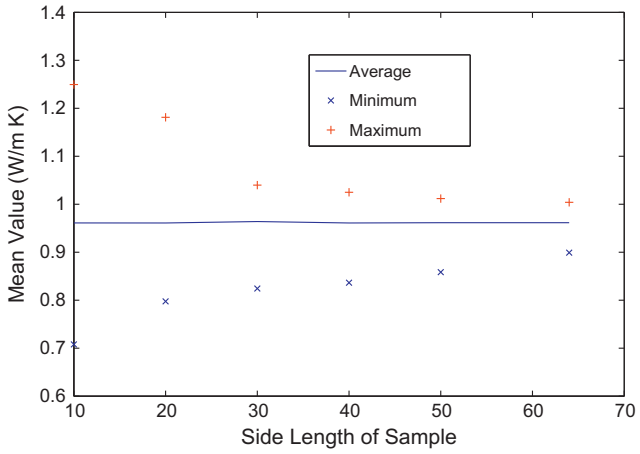

Fig. 6. Effect of sample size on macroscopic mean value of 150 statistical samples.

150 statistical tests as a function of the sample size, where the mean value is observed to converge rapidly. The standard deviation of statistical tests decreases while enlarging the size of sample, see Fig. 7. Clearly, the macroscopic property of a larger sample is more reliable. However, the standard deviation of the sample size of $64^3\ \mu m^3$ is already small enough (see Fig. 7), which is chosen as the RVE for thermal homogenization in this contribution. The mean value and standard deviation are expressed through:

$$K^{mean} = \frac{1}{n}\sum_{i=1}^{n} < K_i > \qquad (17)$$

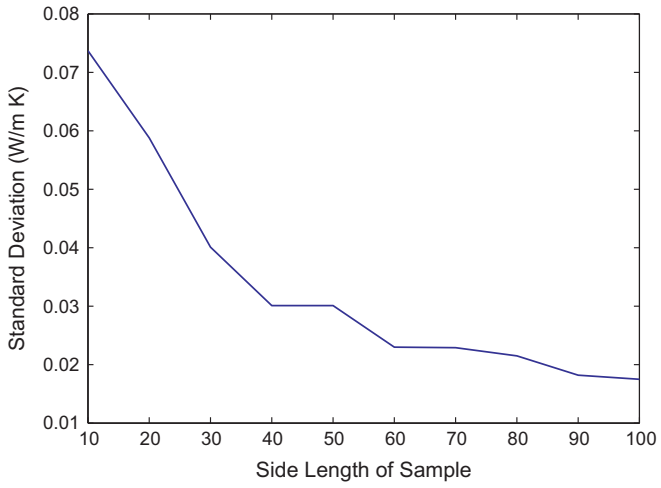

Fig. 7. Effect of sample size on macroscopic standard deviation of 150 statistical samples.

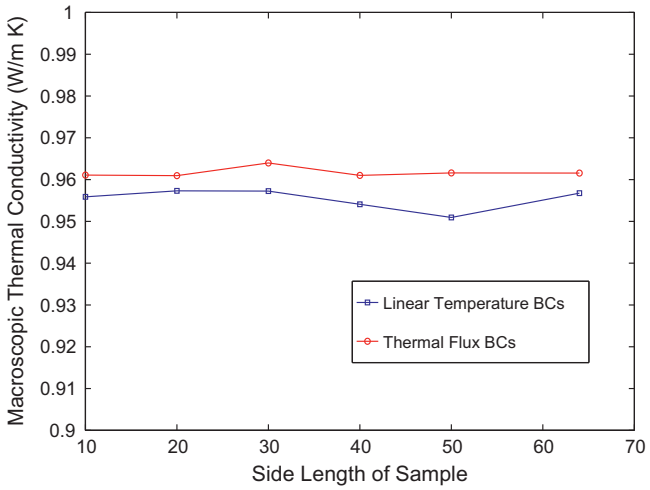

Fig. 8. Effect of types of boundary conditions on macroscopic value of 150 statistical samples.

$$K^{dev} = \sqrt{\frac{1}{n-1}\sum_{i=1}^{n}[< K_i > - K^{mean}]^2} \tag{18}$$

Influence of different types of boundary conditions on the effective thermal conductivity of a single small sample is obviously higher. When the size of the sample is increased, the results from different types of boundary conditions are expected to converge to a limit, see Fig. 8, where 150 randomly chosen samples have been tested under linear temperature and thermal flux boundary conditions. Apparently, results from thermal flux boundary conditions are slightly smaller than the one under linear temperature boundary conditions, which will be explained in the next section.

3.4. Partitioning principle

As mentioned before, linear temperature boundary conditions (LT-BCs) and uniform thermal flux boundary conditions (UF-BCs) satisfy the Hill criterion. Both types of boundary conditions could be applied either in an average thermal flux controlled or average temperature gradient controlled manner [27]. One can show that $K^*_{UF} \leqslant K^*_{LT}$ through the principle of minimum complementary potential dissipation [28]. This result supports the numerical results summarized in Fig. 8 where it is observed that the macroscopic thermal conductivity under UF-BCs is smaller than the one under LT-BCs. On the other hand, when the original sample V is partitioned into a set of smaller subdomains $V' \leqslant V$ and tested under linear temperature boundary conditions, one can show that $K^*_{LT} \leqslant K^{*\prime}_{LT}$ through the principle of minimum potential dissipation [28]. The above inequality additionally supports the numerical results in Fig. 6 where it is observed that the macroscopic property follows the decreasing convergence curve under linear temperature boundary conditions when the size of the sample is increased. Details of the relevant derivations may be found in [27–30].

Table 2
Results of 8000 statistical tests.

Mean value μ (W/m K)	Standard deviation σ (W/m K)
0.9568	0.0257

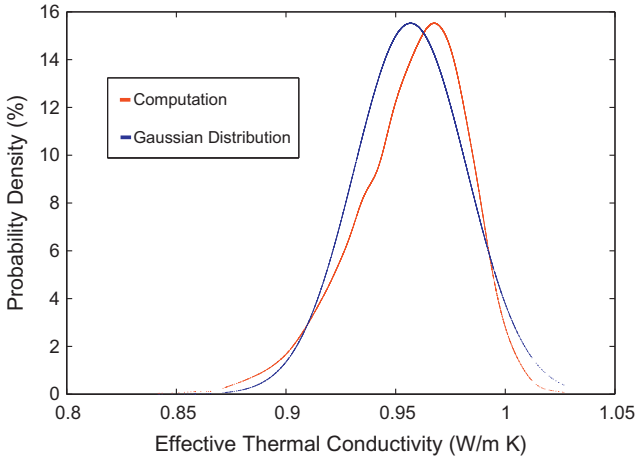

Fig. 9. 8000 Statistical tests distribution and Gaussian distribution.

3.5. Statistical tests

8000 randomly selected RVEs of size 64^3 μm^3 with a window width of 4 μm were tested. Table 2 shows the mean value and the standard deviation of the statistical tests. The probability density of the results is very close to the Gaussian distribution, see Fig. 9.

3.6. Analytical bounds in the microscale

Analytical homogenization approaches, which rely on the volume fraction and thermal properties of the individual components, can only deliver estimates or bounds for the effective property. Nevertheless, they are of interest since the numerical effective property obtained through computational homogenization is bounded by Voigt and Reuss estimates [3,4]:

$$K^{Voigt} \leqslant K^*_{iso} \leqslant K^{Reuss} \tag{19}$$

$$K^{Voigt} = V_H \cdot K_H + V_U \cdot K_U + V_M \cdot K_M = 0.9682 \tag{20}$$

$$K^{Reuss} = (V_H \cdot (K_H)^{-1} + V_U \cdot (K_U)^{-1} + V_M \cdot (K_M)^{-1})^{-1} = 0.9326 \tag{21}$$

Here, H, U and M stand for hydration product, unhydrated clinker and micropore respectively, and V is the volume fraction. The bounds in (19) are demonstrated by the data in Eqs. (20) and (21) and Table 2. One also can observe that the mean value of

statistical tests is quite close to the Voigt bound and individual values are likely to exceed this bound considering the standard deviation in Table 2. This inconsistency with the bounds is due to the fact that the underlying assumption of macroscopic isotropy is violated particularly at small sample sizes.

3.7. Comparison with experimental data of cement paste

Fig. 10 shows the comparison between the computed mean value of 8000 randomly distributed RVEs and the experimental data. In the experiment [23], a thermal constants analyzer, which includes a variety of transient plane source probes connected to a computerized control unit, is used to measure the thermal conductivity of cement paste as a function of hydration degree at 20 °C. All cement pastes were prepared using Cement and Concrete Reference Laboratory (CCRL) cement proficiency sample with $w/c = 0.4$ and over saturated condition. In Fig. 10, one can observe that the hydration degree has a minor effect on the measured thermal conductivity and the computed values with the hydration degree of 0.945 are generally in the same region with the experimental data [23], particularly when the factor of standard deviation is considered. The computed values from Table 2 underestimate the experimental data from [31], which used the photoacoustic technique to measure the effective thermal conductivity of HCP with $w/c = 0.4$ and 0.5, after the fresh cement paste was cured for one month under room temperature. It is known that the pore width gets larger as the w/c increases, which results in lower thermal conductivity [31], as red triangles in Fig. 10 indicate. Since the type of HCP in the numerical simulation is different from the one in [31], it is a possible reason for why the computed results underestimate the experiment data from [31]. In addition, the thermal conductivity of HCP is also sensitive to the water content in pores, as will be investigated next. Nevertheless, all computational results are of the same order of magnitude with experimental observations.

4. Effect of relative humidity on effective conductivity of HCP

4.1. Introduction to the effect of water content in micropores

HCP is a complex porous material and its thermal conductivity can be affected by different factors, such as variation of porosity, high temperature, water content in pores, porosities and mechanical degradation. In recent years, impacts of high temperature on the thermal conductivity of cement paste and concrete were well investigated [32–34]. Presently, the influence of high temperature is not considered, a situation that would be of interest when concrete is attacked by fire. In this contribution, the emphasis is given to the effect of water content changes in micropores of HCP on the thermal property of HCP.

Table 3
Thermal conductivity of components in micropores.

Material	Thermal conductivity (W/m K)
Water	0.604 [23]
Air	0.025 [37]

Here, the pore is simply considered as a mixture of water and the gaseous phase of air. The thermal conductivity of the pore is determined by a modification of the Reuss–Voigt type estimates, namely the Lichtenecker's equation [35,36]

$$K^m_{pore} = V_{air}K^m_{air} + V_{water}K^m_{water}. \tag{22}$$

Here, m is the mode parameter within the range of $[-1,1]$, such that the range from the Reuss bound with $m = -1$ to the Voigt bound with $m = 1$ is captured. The thermal conductivities of air and water are listed in Table 3.

4.2. Comparison with experimental data of cement paste considering the effect of water content in micropores

The values (1.0, −1.0, 0.5, −0.5) for m in Eq. (22) are selected respectively and the estimated thermal conductivity of the micropore is summarized in Fig. 11. Subsequently, for each value of m, computational homogenization is carried out as a function of water volume fraction. For a given microstructural sample, the effective thermal conductivity of HCP qualitatively reflects a similar response as Fig. 11, see Fig. 12. 150 statistical tests were additionally conducted for each value of m as a function of water volume fraction, see Fig. 13. Fig. 14 illustrates a comparison between the computed results for $m = 1$ and the experimental data. In this experiment [38], TLPP (two-linear-parallel-probe) method was used to determine the thermal conductivity of HCP with $w/c = 0.35$ and 0.4 under dry and wet conditions respectively. Two probes were inserted into two parallel holes drilled in the specimen, where one probe was used as a heating source and the other as a temperature sensor [38]. It is assumed that the volume fraction of water in the pore is 0% for the dry condition and 100%

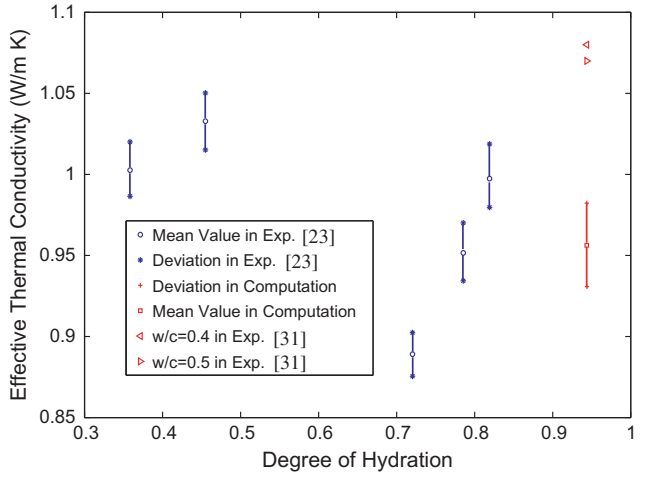

Fig. 10. Computed effective thermal conductivity of HCP and experimental data of cement paste.

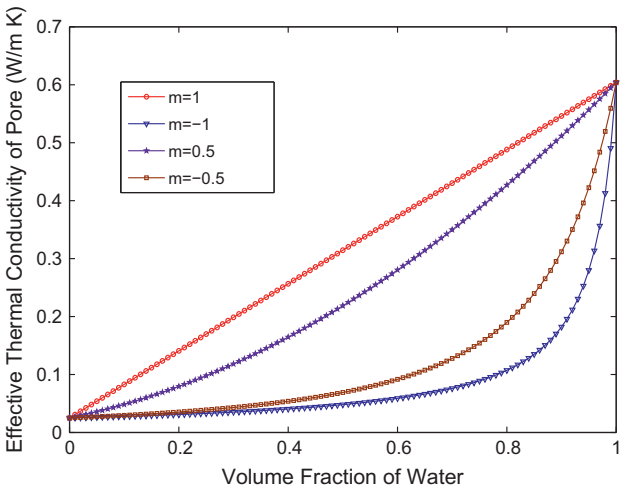

Fig. 11. Analytical thermal conductivity of micropore.

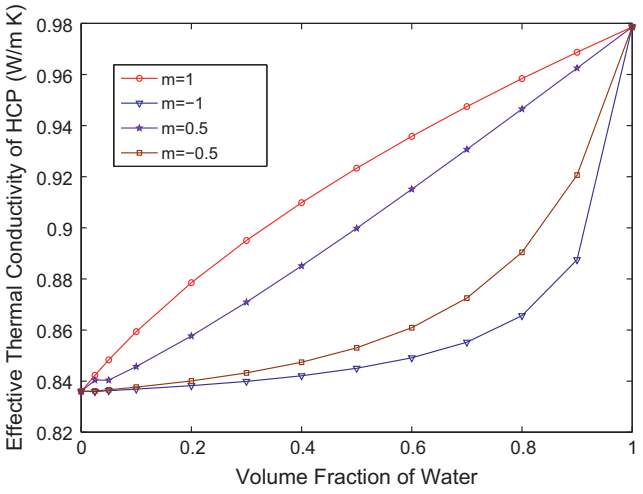

Fig. 12. Effective thermal conductivity of one single RVE of HCP with respect to different volume fractions of water in micropores.

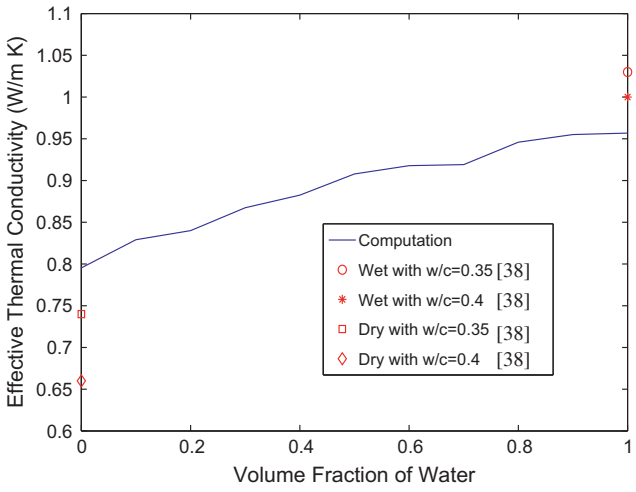

Fig. 14. Computed effective thermal conductivity of HCP with respect to volume fraction of water in micropore and experimental results of cement paste.

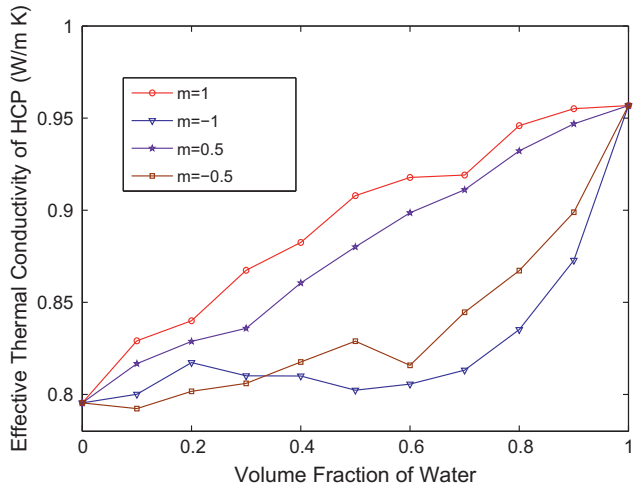

Fig. 13. Effective thermal conductivity of 150 statistical RVEs of HCP with respect to different volume fractions of water in micropores.

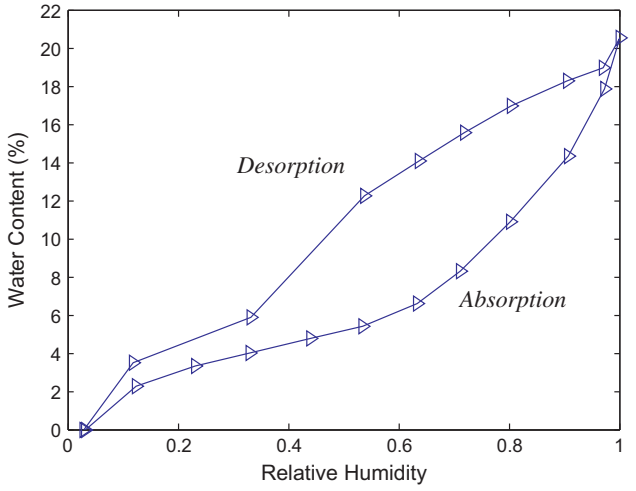

Fig. 15. Isothermal absorption–desorption [39].

for the wet condition. This never occurs in reality, since hydrostatic pressure enables the release of the trapped air from the pores and the hygroscopic range of saturation is up to 97%. In addition, capillary saturation and pores with a radius smaller than 1 μm are neglected. All mentioned above reasons can seemingly explain the difference between experimental data and computed values. Unfortunately, experimental data on the thermal conductivity of cement paste between a dry state and a wet state is not available.

4.3. Absorption and desorption

Mechanisms of absorption and desorption are very common in the porous material, where a substance is absorbed or released by another substance. Aforementioned issues result in the isothermal desorption and absorption curves for HCP with $w/c = 0.45$ in Fig. 15, which can be clarified by physical mechanisms, such as molecular absorption/desorption, capillary condensation, surface tension and disjoining pressure [39]. A typical experiment is performed through the saturated salt solution method where the specimens are kept in sealed cells under constant temperature [39]. Here, the relative humidity is kept constant by means of a saturated salt solution and the specimens are subjected to step-by-step desorption and subsequent absorption processes. In addition, various physically-based models have been developed to account for absorption/desorption isotherms, in order to understand the physics of confined systems and to predict their behavior. Further results on HCP and concrete may be found in [39–41]. Water content of HCP under the same relative humidity is higher at desorption isotherm than the one at absorption isotherm, which is explained by the fact that the physical and chemical structures of cement paste are changed due to partial collapse of pore structure during first drying.

The relative saturation degree is defined as the current water content by the saturated water content in Fig. 15, which has the same physical meaning as the volume fraction of water used in previous computation steps. One can map the obtained curve of Fig. 14 from the volume fraction of water to the relative humidity through isothermal absorption curve, since the relative humidity is widely applied in chemical reaction models. The mean value and standard deviation with respect to the relative humidity are illustrated in Figs. 16 and 17, where the approximations are obtained through

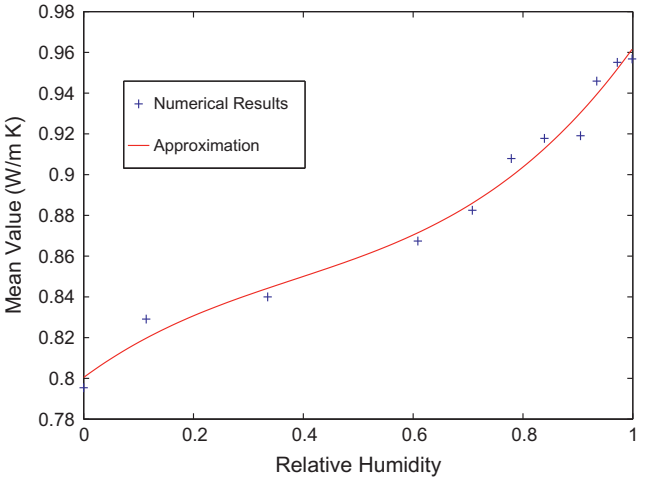

Fig. 16. Mean value of effective thermal conductivity of HCP with respect to relative humidity of water in micropore and polynomial approximation.

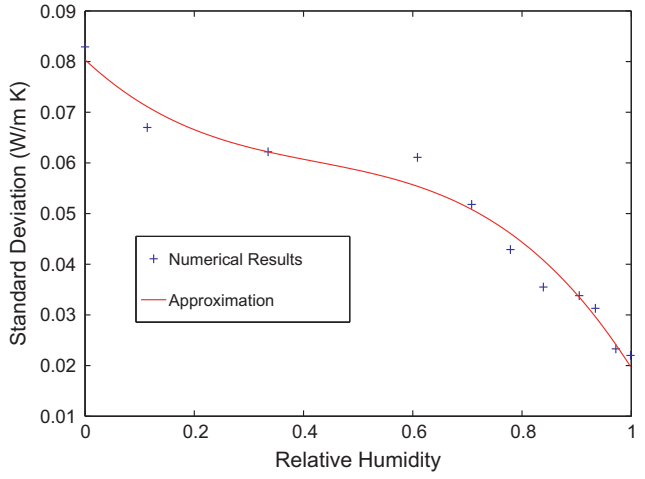

Fig. 17. Standard deviation of effective thermal conductivity of HCP with respect to relative humidity of water in micropore and polynomial approximation.

Table 4
Coefficients of approximation for effective thermal conductivity of HCP as a function of relative humidity.

i	0	1	2	3
Mean (a_i^{med})	0.8005	0.1985	−0.2860	0.2491
Deviation (a_i^{dev})	0.0804	−0.1008	0.1886	−0.1486

$$K(h)^{med} = \sum_{i=0}^{i\leqslant 3} a_i^{med} h^i \tag{23}$$

$$K(h)^{dev} = \sum_{i=0}^{i\leqslant 3} a_i^{dev} h^i \tag{24}$$

with h as the relative humidity and a_i as coefficients of approximations listed in Table 4. One can directly upscale the effect of relative humidity in the microscale to the mesoscale.

5. Computational homogenization in the mesoscale

Randomly distributed aggregates in the homogenized HCP consists the mesoscale of concrete, where the size and the statistical

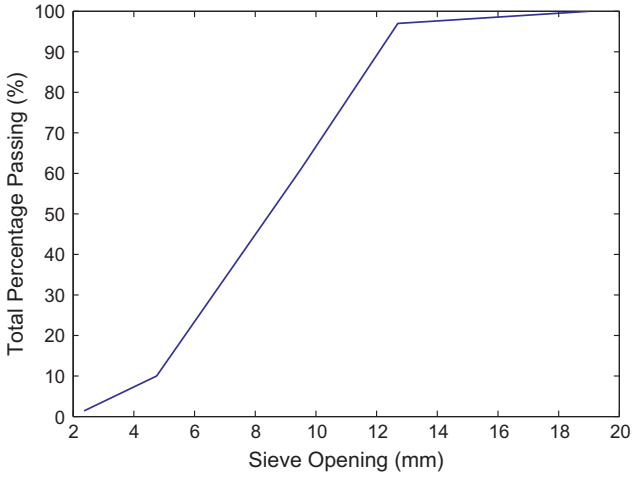

Fig. 18. Grading curve of aggregates.

Table 5
Aggregate size distribution.

Size (mm)	Retained (%)	Passing (%)
19.00	0	100
12.70	3	97
9.50	39	61
4.75	90	10
2.36	98.6	1.4

distribution of the aggregates must resemble the original concrete itself. The way to generate a realistic aggregate arrangement was well developed in the past 50 years. Numerous applications of the take-and-place method were introduced for low aggregate volume fractions by Wang et al. [42], Wriggers and Moftah [43] and others. Alternatively, De Schuter and Taerwe [44] used the divide-and-fill method for higher aggregate volume fractions. Limestone, quartz and sand are the primary aggregates used, the total volume fraction of which is 60–80% in engineering applications.

5.1. Take-and-place algorithm

The take-and-place method employed in this work can be explained in two steps. The first step is to obtain the list of radii of randomly distributed aggregates from a source, the size distribution of which follows a certain grading curve in Fig. 18 and Table 5. The second step is to place aggregates one by one into HCP, while guaranteeing no overlap with previously placed particles as well as with the boundary of HCP. In practice, concrete is widely designed according to the Fuller curve which can yield the optimal density and the strength of concrete. The employed grading curve of Fig. 18 has previously been made use of by Wriggers and Moftah [43]. In the end, four representations with volume fractions of 10%, 30%, 50% and 60% are demonstrated in Fig. 19.

The quality of a finite element discretization of the concrete including aggregates and HCP directly affects the accuracy of the numerical simulation. Basically there are two approaches to mesh it: the unaligned or aligned approach. In the aligned meshing approach, the finite element mesh can match geometrical boundaries between aggregates and matrix. Unaligned meshing approach does not have this advantage, leading to loss of accuracy, although the precision of the numerical simulation may be partially improved by increasing the number of integration points at the interface [12]. In this work, the generated mesostructure model is transferred into the software CUBIT which offers the option of automatic

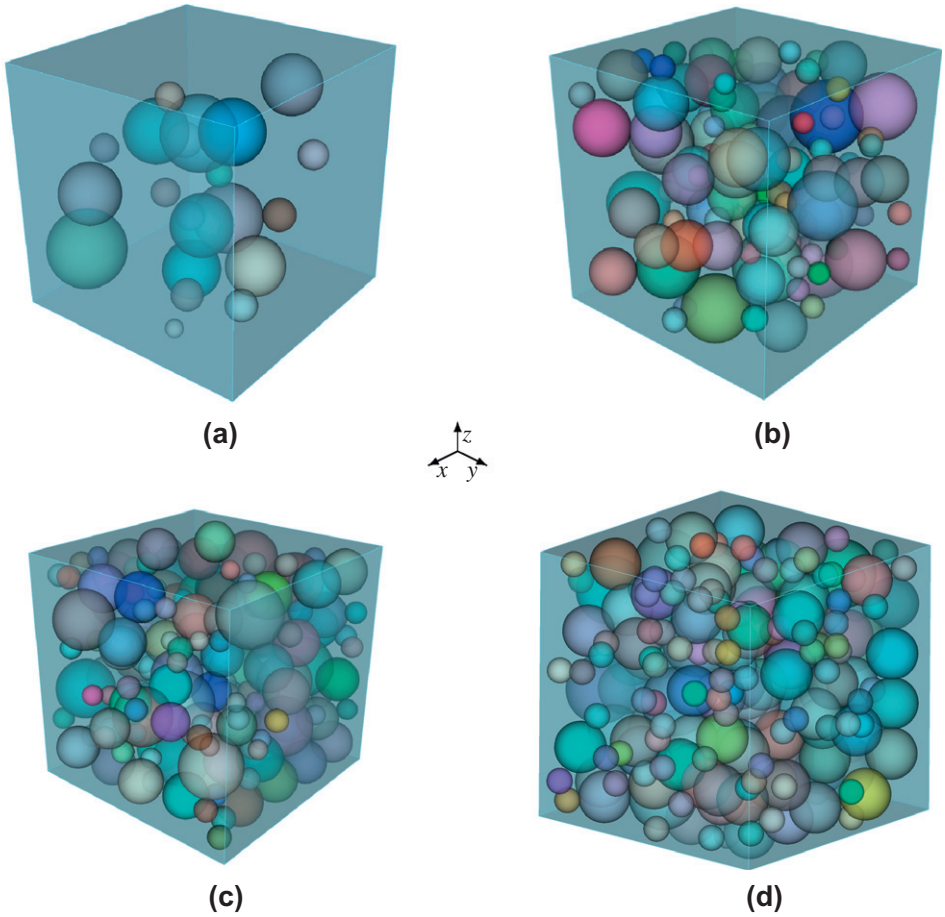

Fig. 19. (a) Volume fraction of aggregates with 10%, (b) volume fraction of aggregates with 30%, (c) volume fraction of aggregates with 50%, and (d) volume fraction of aggregates with 60%.

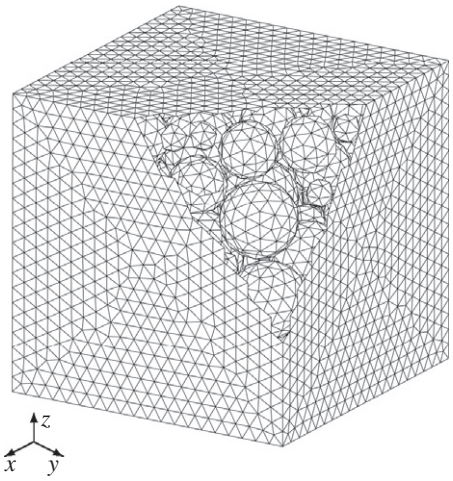

Fig. 20. Finite element mesh of mesoscale (coarse mesh).

mesh generation with tetrahedral elements in the manner of the aligned approach (see Fig. 20), and then one can output the mesh file to the finite element analysis program (FEAP) for the numerical homogenization [45].

5.2. Numerical simulation in the mesoscale

As mentioned before, types of aggregates play an important role on the physical property of the concrete. Thermal conductivities of some general types of aggregates are listed in Table 6. Their average value is used to represent the thermal conductivity of aggregates in this contribution. The thermal conductivity of HCP matrix, in turn, from the mean value of 8000 statistical tests (Section 3.5), which generates the link between the microscale and the mesoscale and clarifies the physical meaning of multiscale. The objective of the test in Fig. 21) is to highlight the thermal flux distribution in the mesoscale of concrete, where constant temperature boundary conditions are prescribed on the top. Aggregates are close to each other and the thermal conductivity of aggregates is higher, thereby leading to efficient paths of conduction across an aggregate chain. The next step is to impose the linear temperature boundary conditions to initialize the work of homogenization through Eqs. (2) and (3). For this case, the effective thermal conductivity with respect to different volume fractions of aggregates is listed in Table 7. The effect of relative humidity changes in micropores on the effective thermal conductivity of HCP has already been investigated in Fig. 16, which could be incorporated

Table 6
Thermal conductivity of general grounds [46].

Type of ground	Thermal conductivity (W/m K)
Quartz	4.45
Granite	2.50–2.65
Limestone	2.29–2.78
Marble	2.11
Basalt	2.47

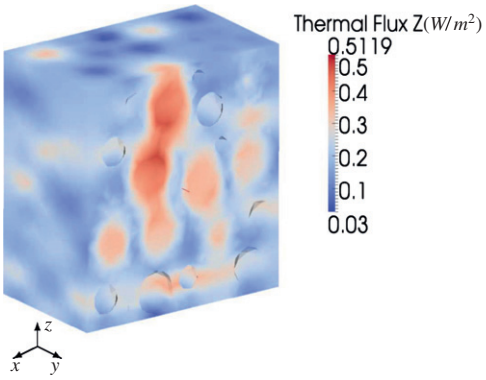

Fig. 21. Thermal flux in the mesoscale (cross-section shown).

Table 7
Computed effective thermal conductivity of concrete.

Volume fraction (%)	Effective thermal conductivity (W/m K)
10	1.073
30	1.343
50	1.667
60	1.750

into the framework of thermal homogenization in the mesoscale, since effective thermal conductivity of HCP affects the one of HCP. Eventually, one can obtain the nonlinear effective thermal conductivity of concrete relying on relative humidity changes in the micropores, see Fig. 23, which establishes the link between the nonlinear effect of relative humidity in the microscale and the macroscopic thermal property of concrete.

5.3. Analytical bounds in the mesoscale

Voigt and Reuss bounds of thermal conductivity of concrete [3,4] are obtained through:

$$K^{Voigt}_{concrete} = V_{HCP}K_{HCP} + V_{aggregate}K_{aggregate} \tag{25}$$

$$K^{Reuss}_{concrete} = (V_{HCP}(K_{HCP})^{-1} + V_{aggregate}(K_{aggregate})^{-1})^{-1} \tag{26}$$

The analytical bounds of thermal conductivity of concrete with respect to different volume fractions of aggregates are listed in Table 8, which provide the bounds for numerical results in Table 7.

5.4. Comparison with experimental data of concrete

After the initialization of computational thermal homogenization, the effective thermal conductivity with respect to different volume fractions of aggregates are evaluated (see Table 7). Fig. 22 presents the comparison between experimental data and computed values. In the experiment [46], QTM-D3 device was used to measure the thermal conductivity of concrete through the probe method, where concrete specimens with different volume fraction of aggregates were subjected to moisture curing and dry curing. There is no doubt that the thermal conductivity of concrete is increased as the volume fraction of aggregates rises, due to higher thermal conductivity of aggregates. Since the thermal homogenization of HCP delivers the thermal conductivity of the matrix in the mesoscale of concrete, where the saturated condition for the micropore of HCP was considered, one can observe that the numerical results coincide with wet experimental data [46]. Experimental data from [47] provides the lower and upper limits. The simulated value is located in the experimental range.

Table 8
Analytical bounds of thermal conductivity of concrete.

Volume fraction (%)	Voigt estimate (W/m K)	Reuss estimate (W/m K)
10%	1.1439	1.0246
30%	1.5182	1.1938
50%	1.8924	1.4298
60%	2.0795	1.5867

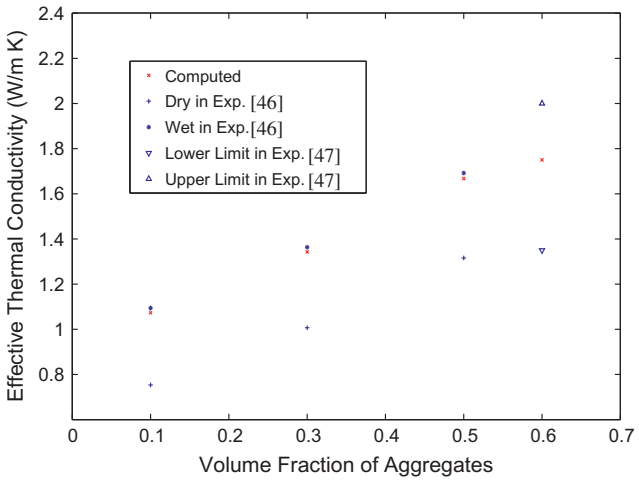

Fig. 22. Computed effective thermal conductivity of mesoscale and experimental results of concrete.

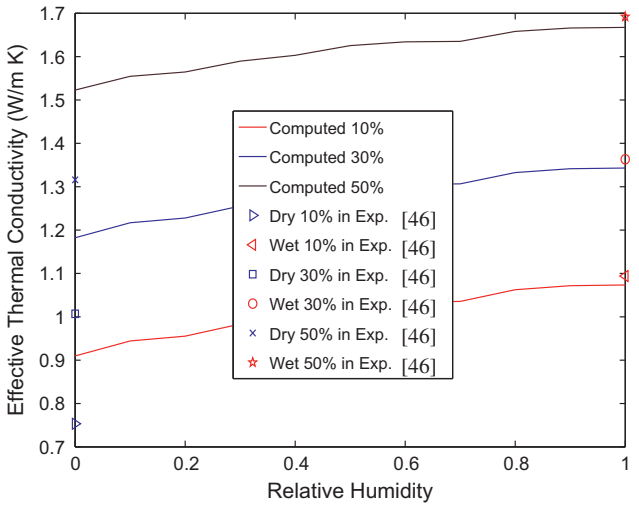

Fig. 23. Computed effective thermal conductivity of mesoscale considering the effect of relative humidity from microscale and experimental results of concrete.

The homogenization of HCP delivers the effective thermal conductivity of the matrix in the mesoscale, and this effective value may be parametrized as a function of the relative humidity in the micropores. Therefore, this parametrization may subsequently be used to reflect the relative humidity effect to the mesoscale analysis with the aggregates, see Fig. 23. A comparison of these computational results with the experiments is not straightforward. For instance, the framework of experiment [44] has been introduced above but it only supplies data for the extreme states of completely dry or wet concrete samples, with no information on intermediate states. One can observe that the calculated results match the wet end of the data very well but not the dry end.

One possible reason for this discrepancy is the fact that mesoscale pores have been neglected from the analysis. In reality, some portions of the solid matrix should be replaced by pores. Since the thermal conductivity of completely wet pores is very close to that of the matrix, this approximation does not significantly alter the conductivity of the wet concrete but overestimates the conductivity of the dry concrete. Nevertheless, the results are observed to be of the same order of magnitude.

6. Conclusion

In this contribution, 3D micro-CT scan of hardened cement paste (HCP) and aggregates with a random distribution embedded in a homogenized HCP were used to represent the microscale and mesoscale of concrete respectively, overall offering a multiscale analysis framework. In the microscale, computational homogenization with statistical tests was applied to obtain the effective thermal conductivity of HCP. Due to the variation of water content in the micropores, a nonlinear relationship between the effective thermal conductivity of HCP and the volume fraction of water content in micropores was observed. This nonlinear relationship was then mapped from the volume fraction of water content to the relative humidity through the isothermal curve of absorption.

In the mesoscale, the take-and-place algorithm was used to generate randomly distributed aggregates embedded in the homogenized HCP. Computational thermal homogenization with respect to different volume fractions of aggregates was performed. Furthermore, the effect of water content changes in the microscale was also upscaled to the mesoscale.

By using computational thermal homogenization, one can identify the macroscopic thermal conductivity of concrete efficiently. This framework is inexpensive, fast, and not restricted by space and time, compared with the conventional experimental approach. In addition, the framework conveniently incorporates the effect of relative humidity changes in the micropores on the macroscopic thermal conductivity of concrete. The ability to capture such effects is of significant importance in modeling long term temperature-controlled chemical reactions in concrete, such as the alkali silica reaction. Finally, it is of interest to account for thermomechanical coupling in the context of damage initiation and subsequent progression towards interface fracture. Such investigations are currently being pursued by the authors.

Acknowledgments

The authors thank Michael Hain for offering the mesh of hardened cement paste and Dale P. Bentz in the Engineering Laboratory of the National Institute of Standards and Technology for providing specific experimental parameters.

References

[1] http://www.understanding-cement.com/alkali-silica.html.
[2] Tong L, Tang MS. Correlation between reaction and expansion of alkali-carbonatereaction. Cem Concr Res 1995;25(3):47076.
[3] Voigt W. Über die beziehung zwischen den beiden elastizitätskonstanten isotroper körper. Wied Ann 1889;38:573–87.
[4] Reuss A. Berechnung der fliessgrenze von mischkristallen auf grund der plastizitätsbedingung für einkristalle. Z Angew Math Mech 1929;9:49–58.
[5] Hill R. A self-consistent mechanics of composite materials. J Mech Phys Solids 1965;13(4):213–22.
[6] Dai LH, Huang ZP, Wang R. A generalized self-consistent Mori-Tanaka scheme for piction of the effective elastic moduli of hybrid multiphase particulate composites. Polym Compos 1998;19(5):506–13.
[7] Mori T, Tanaka K. Average stress in matrix and average elastic energy of materials with misfitting inclusions. Acta Metall 1973;21(5):571–4.
[8] Sauermann G, Turschner H, Just W. Selfconsistent approximations in Mori's theory. Physica A 1997;225(1):19–61.
[9] Miehe C, Koch A. Computational micro-to-macro transitions of discretized microstructures undergoing small strains. Arch Appl Mech 2002;72(4–5):300–17.
[10] Miehe C, Schröder J, Schotte J. Computational homogenization analysis in finite plasticity simulation of texture development in polycrystalline materials. Comput Methods Appl Mech Eng 1999;171(3–4):387–418.
[11] Temizer İ, Zohdi TI. A numerical method for homogenization in non-linear elasticity. Comput Mech 2007;40(2):281–98.
[12] Zohdi TI, Wriggers P. An introduction to computational micromechanics. Springer; 2005.
[13] Asakuma Y, Miyauchi S, Yamamoto T, Aoki H, Miura T. Homogenization method for effective thermal conductivity of metal hydride bed. Int J Hydrogen Energy 2004;29(2):209–16.
[14] Laschet G, Sauerhering J, Reutter O, Fend T, Scheele J. Effective permeability and thermal conductivity of open-cell metallic foams via homogenization on a microstructure model. Comp Mater Sci 2009;45:597–603.
[15] Zhang HW, Zhou Q, Xing HL, Muhlhaus H. A DEM study on the effective thermal conductivity of granular assemblies. Powder Technol 2011;205(1–3):172–83.
[16] Temizer İ, Wriggers P. A micromechanically motivated higher-order continuum formulation of linear thermal conduction. Z Angew Math Mech 2010;90(10–11):768–82.
[17] Nemat-Nasser S, Hori M. Micromechanics: overall properties of heterogeneous materials. Springer; 2005.
[18] Krabbenhoft K, Hain M, Wriggers P. Computation of effective cement paste diffusivities from microtomographic images. In: Kompis V, editor. Composites with micro- and nano-structure, vol. 9; 2008. p. 281–97.
[19] Acker P. Micromechanical analysis of creep and shrinkage mechanisms. In: Creep, shrinkage and durability mechanics of concrete and other quasi-brittle materials: proceedings of the sixth international conference, vol: 1; 2001. p. 15–25.
[20] Hain M, Wriggers P. Numerical homogenization of hardened cement paste. Comput Mech 2008;42(2):197–212.
[21] Ye G. Experimental study & numerical simulation of the development of the microstructure and permeability of cementitious materials. Phd thesis. Delft, Delft University of Technology; 2003.
[22] Bentz DP. Three-dimensional computer simulation of portland cement hydration and microstructure development. J Am Ceram Soc 1997;80(1):3–21.
[23] Bentz DP. Transient plane source measurements of the thermal properties of hydrating cement pastes. Mater Struct 2007;40(10):1073–80.
[24] Powers TC. Physical properties of cement paste. In: 4th International symposium on the chemistry of cement; Paper V-1: physical properties of cement paste, vol: 2(43); 1962. p. 577–613.
[25] Hain M, Wriggers P. Computational homogenization of micro-structural damage due to frost in hardened cement paste. Finite Elem Anal Des 2008;44(5):233–44.
[26] Bentz DP. CEMHYD3D: a three-dimensional cement hydration and microstructural development modelling package, version 2.0, NISTIR 6485, US Department of Commerce 2000; <http://ciks.cbt.nist.gov/bentz/cemhyd3dv20>.
[27] Huet C. Application of variational concepts to size effects in elastic heterogeneous bodies. J Mech Phys Solids 1990;38(6):813–41.
[28] Ostoja-Starzewski M. Microstructural randomness versus representative volume element in thermomechanics. J Appl Mech 2002;69(1):25–35.
[29] Rosen BW, Hashin Z. Effective thermal expansion coefficients and specific heats of composite materials. Int J Eng Sci 1970;8(2):157–73.
[30] Torquato S. Random heterogeneous materials. Springer; 2001.
[31] Abdelalim A, Abdallah S, Easawi K, Negm S, Talaat H. Thermal properties of hydrated cement pastes studied by the photoacoustic technique. In:15th International conference on photoacoustic and photothermal phenomena (ICPPP15), Leuven, Belgium, July 19–23; 2009.
[32] Hu XF, Lie TT, Polomark GM, Maclaurin JW. Thermal properties of building materials at elevated temperatures. Internal report; 1993.
[33] Kodur V, Khaliq W. Effect of temperature on thermal properties of different types of high-strength concrete. J Mater Civil Eng 2011;23(6):793–802.
[34] Shin KY, Kim SB, Kim JH, Chung M, Jung PS. Thermo-physical properties and transient heat transfer of concrete at elevated temperatures. Nucl Eng Des 2002;212(1–3):233–41.
[35] Č.erný R, Pavlík Z. Homogenization techniques for determination of thermal conductivity of porous materials. In: Proceedings of Thermophysics (Kočovce, Slovak Rep.), STU Bratislava; 2007. p. 76–80.
[36] Pavlík Z, Vejmelková E, Fiala L, Černý R. Effect of moisture on thermal conductivity of lime-based composites. Int J Thermophys 2009;30(6):1999–2014.
[37] Carson JK, Lovatt SJ, Tanner DJ, Cleland AC. Experimental measurements of the effective thermal conductivity of a pseudo-porous food analogue over a range of porosities and mean pore sizes. J Food Eng 2004;63(1):87–95.
[38] Jeon SE, Kim JK. Analysis of concrete structures with hydration heat and differential shrinkage. PhD thesis, Daejeon, Korea Advanced Institute of Science and Technology; 2008.
[39] Baroghel-Bouny V. Water vapour sorption experiments on hardened cementitious materials: Part I: essential tool for analysis of hygral behaviour and its relation to pore structure. Cem Concr Res 2007;37(3):414–37.
[40] Rougelot T, Skoczylas F, Burlion N. Water desorption and shrinkage in mortars and cement pastes: experimental study and poromechanical model. Cem Concr Res 2009;39(1):36–44.

[41] Tada S, Watanabe K. Dynamic determination of sorption isotherm of cement based materials. Cem Concr Res 2005;35(12):2271–7.
[42] Wang ZM, Kwan AKH, Chan HC. Mesoscopic study of concrete I: generation of random aggregate structure and finite element mesh. Comput Struct 1999;70(5):533–44.
[43] Wriggers P, Moftah SO. Mesoscale models for concrete: homogenisation and damage behaviour. Finite Elem Anal Des 2006;42(7):623–36.
[44] De Schutter G, Taerwe L. Random particle model for concrete based on Delaunay triangulation. Mater Struct 1993;26(2):67–73.
[45] FEAP. A finite element analysis program (R.L. Taylor).
[46] Kim KH, Jeon SE, Kim JK, Yang S. An experimental study on thermal conductivity of concrete. Cem Concr Res 2003;33(3):363–71.
[47] Eurocode. Design of concrete structures, Part 1.2. General rules-structural fire design (EN1992-1-2). Commission of European Communities, Brussels; 2004.